Investigation on Porosity and Microhardness of 316L Stainless Steel Fabricated by Selective Laser Melting

Shahir Mohd Yusuf [1], Yifei Chen [1], Richard Boardman [2], Shoufeng Yang [1] and Nong Gao [1,*

[1] Materials Research Group, Faculty of Engineering and the Environment, University of Southampton, Southampton SO17 1BJ, UK; symy1g12@soton.ac.uk (S.M.Y.); chenyifeiuk@sina.com (Y.C.); S.Yang@soton.ac.uk (S.Y.)

[2] μ-VIS X-Ray Imaging Centre, Faculty of Engineering and The Environment, University of Southampton, Southampton SO17 1 BJ, UK; rpb@soton.ac.uk

* Correspondence: n.gao@soton.ac.uk; Tel.: +44-23-8059-3396

Abstract: This study investigates the porosity and microhardness of 316L stainless steel samples fabricated by selective laser melting (SLM). The porosity content was measured using the Archimedes method and the advanced X-ray computed tomography (XCT) scan. High densification level ($\geq$99%) with a low average porosity content (~0.82%) were obtained from the Archimedes method. The highest porosity content in the XCT-scanned sample was ~0.61. However, the pores in the SLM samples for both cases (optical microscopy and XCT) were not uniformly distributed. The higher average microhardness values in the SLM samples compared to the wrought manufactured counterpart are attributed to the fine microstructures from the localised melting and rapid solidification rate of the SLM process.

1. Introduction

Additive manufacturing (AM) is an advanced manufacturing process which involves layer-wise material addition to fabricate three-dimensional (3D) objects based on pre-defined Computer Aided Design (CAD) data. This technology possesses the advantage of design flexibility, which enables the fabrication of parts with complex geometries and intricate features compared to traditional processes such as casting and forging. In addition, the additive nature of this process allows components to be manufactured with much less raw material wastage which could reduce material costs and the environmental footprint [1,2]. The AM of metal components has evolved from rapid prototyping (RP) to fabrication of functional metallic components for end use such as in the automotive, biomedical and aerospace industries [3,4].

Various AM processes for metals have been well described and reviewed [5,6]. Selective laser melting (SLM) is one of the major AM technologies that has been used to process a number of metals and alloys, e.g., Ti6Al4V [7], β-type Ti–24Nb–4Zr–8Sn [8,9], Ni superalloy [10] and 316L stainless steel (316L SS) [11], for a wide range of applications, including bone implants [12], turbine blades [13] and automotive pistons [3]. In SLM technology, the laser beam is used to completely melt metal powder layers spread on a powder bed to form near-net-shaped components. In this process, 3D models are first sliced into 2D cross-sections with a set thickness value. The laser beam then scans the cross-section of the designed part layer by layer before selectively fusing them on top of each other, which enables the final 3D part to be formed directly.

316L SS, in particular, is highly attractive for biomedical and marine applications due to its excellent corrosion resistance and relatively superior ductility compared to other materials [14–16]. Current research on AM of 316L SS is not only limited to single-material processing, but also extends to composites. For example, Al Mangour et al. [17] studied the SLM of TiC-reinforced 316L SS matrix nanocomposites and found that the addition of fine TiC particles remarkably improved the microhardness and wear performance of the fabricated parts. This is because of the increase in the densification level and the homogeneous microstructure distribution as a result of enhanced reinforcement/matrix wettability. In addition, studies on the SLM of TiB_2/316L SS nanocomposites were also carried out with varying results. For example, superior compression yield strength and ductility were obtained when processing this nanocomposite without a hot isostatic pressing (HIP) post-processing due to the formation of homogenously dispersed TiB2 particles forming nanoscaled structures [18]. However, HIP treatment was found to reduce the hardness and wear resistance due to the high-temperature annealing effect [19]. Nevertheless, the flexibility of AM processes to fabricate such composites provides a promising future, especially for parts requiring complex geometries.

Although SLM is able to manufacture almost fully dense parts (~98%–99%), the presence of residual porosity in SLM-fabricated parts hinders high-strength and fatigue resistance applications [20]. Similar to conventionally manufactured parts, the mechanical properties of components built by SLM are influenced by the resulting microstructure and porosity profiles (size and morphology) [1,21]. Hence, it is important to understand the microstructure and porosity formation and how their behaviour influences the mechanical properties of the completed parts. Thus, this study aims to investigate the microstructure, porosity distribution and microhardness of 316L SS parts fabricated by SLM, in particular by using the advanced X-ray computed tomography (XCT) technique.

2. Materials and Methods

Gas-atomised 316L SS powders (Concept Laser GmbH, Lichtenfels, Germany) with diameters ranging from 15 to 40 μm were used in this study. The as-supplied material composition of this alloy is shown in Table 1. The low P, C and S contents in 316L SS reduce the susceptibility of this material to sensitisation (grain boundary carbide precipitation), in which sensitisation could reduce the mechanical properties of the fabricated parts.

Table 1. Chemical composition (wt. %) of 316L SS powders used in this study.

Component	Fe	Cr	Ni	Mo	Mn	Si	P	C	S
wt. %	Bal.	16.5–18.5	10.0–13.0	2.0–2.5	<2.0	<1.0	<0.045	<0.030	<0.030

All AM 316L SS samples were fabricated by using Concept Laser M2 Laser Cusing SLM machine (Concept Laser GmbH, Lichtenfels, Germany) in an inert gas environment. The processing parameters used in this study were as follow: (i) laser power: 200 W; (ii) scan speed: 1600 mm/s; and layer thickness: 50 μm. The samples were built using the "island" scan strategy to reduce the residual stress in the completed parts (Figure 1) [22,23].

In this study, three samples were fabricated by SLM and one sample was made by using the conventional wrought manufacturing (WM) technique. The SLM samples were built along the *z*–axis (vertically). For optical microscopy, cube-shaped AM samples (originally 8 mm × 8 mm × 8 mm) were cut into 4 mm × 4 mm square cross-sections along the *x*–*y*, *y*–*z* and *x*–*z* planes using a wire electrical discharge machine. They are then mounted on conductive bakelite, ground using 120, 800, and 1200 grits abrasive papers and polished using 6 μm and 1 μm diamond paste to obtain mirror-like surface finish. In order to reveal the microstructures, the polished samples were etched using Kalling's No. 2 reagent (50 mL HCl, 50 mL ethanol, 2 g copper chloride for 100 mL of etchant) for approximately 30 s. Olympus BX41M-LED optical microscope (Tokyo, Japan) was used to observe the microstructure on the metallographic specimens.
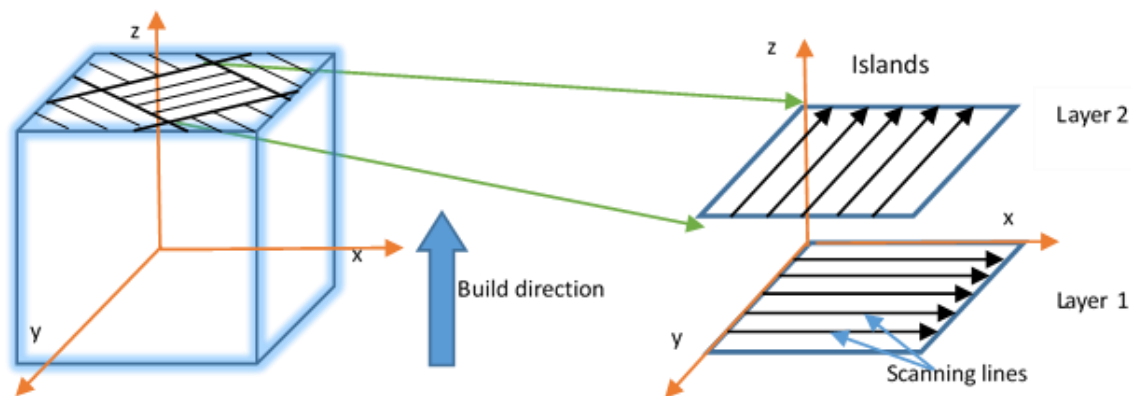
Figure 1. "Island" scanning strategy, shaped like checkerboards employed in the SLM process of 316L SS samples.

Vickers microhardness (HV) measurements were taken along the cross-sections using FM-300 Microhardness Tester (Future-Tech Corp, Kanagawa, Japan). The distance between each indentation was 1 mm and the applied load was 100 gf with dwell time of 10 s. The measurements at each position were repeated three times and the average HV values were calculated. In addition, HV values were also obtained from the cube-shaped 316L SS sample manufactured by WM using similar testing conditions.

The average porosity in the SLM-built samples was calculated using the well-known Archimedes method. On the other hand, the pore size distribution was determined using optical microscopy (GenICam software, Basler AG, Ahrensburg, Germany) from 15 micrographs for each sample. In addition, one AM sample (approximately 10 mm × 10 mm × 15 mm) was subjected to advanced X-ray computed tomography (XCT) scan to obtain information on porosity as this sample had a relatively complex geometry compared to the other samples. This sample was first scanned under low resolution using Nikon Benchtop CT160Xi (Nikon Metrology, Herts, UK) to obtain the general porosity distribution. Then, a small region with the highest porosity content was chosen to undergo detailed scanning using 160 kV Zeiss XRadia 510 Versa (Carl Zeiss Microscopy GmbH, Jena, Germany) with high resolution of 3.2 µm for 20 h. After reconstruction and handling of raw images from the XCT scan results, VG Studio Max software (Volume Graphics GmbH, Heidelberg, Germany) was used as a 3D visualisation tool to obtain detailed porosity distribution in the small region of interest. The porosity in XCT-scanned samples was defined using the Otsu method described in Ref. [24].

3. Results and Discussion

3.1. Microstructure

Figure 2a shows the cross-sectional views on the *x–y* (scan direction) plane, while Figure 2b,c shows the cross-sectional views on the *x–z* and *y–z* planes (build direction), respectively. These melted scan tracks are representative of the solidified melt pool for each layer on the powder bed. The curved "fish-scale"—like geometries observed in the *x–z* and *y–z* (build direction) planes are due to the semi-circular shape of the melt pool and the partial re-melting of successively deposited layers which have been solidified [23]. These overlapping geometries also demonstrate successful fusion of powder particles and bonding within each layer, similar to the work carried out by Cherry et al. [1] and Yasa and Kruth [20].
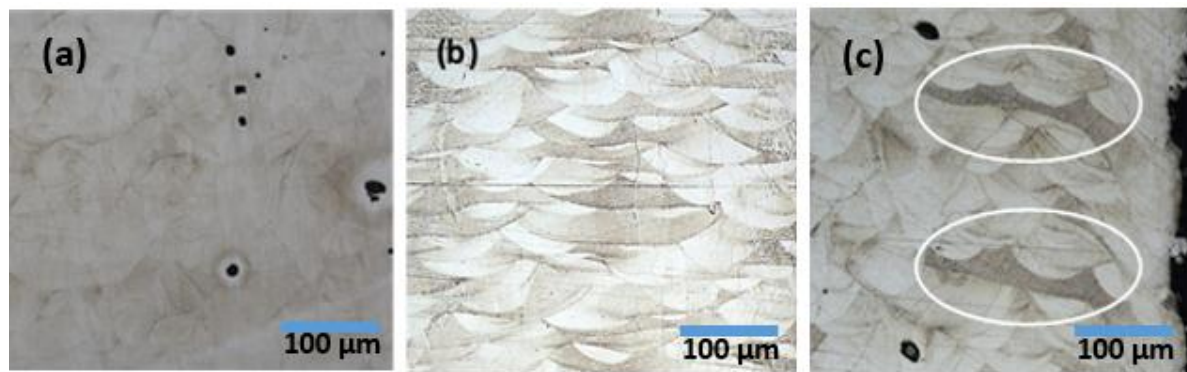
Figure 2. Cross-sectional views of SLM samples on (**a**) *x–y* plane; (**b**) *x–z* plane; and (**c**) *y–z* plane.

A fine cellular-dendritic microstructure could be observed in the SLM-fabricated samples as shown in Figure 3. This is a common characteristic for metal materials fabricated by AM processes as a result of the rapid solidification rates in the locally melted areas (selectively laser-scanned regions) which were experienced because of short laser-material interaction time during the build process [25–27].
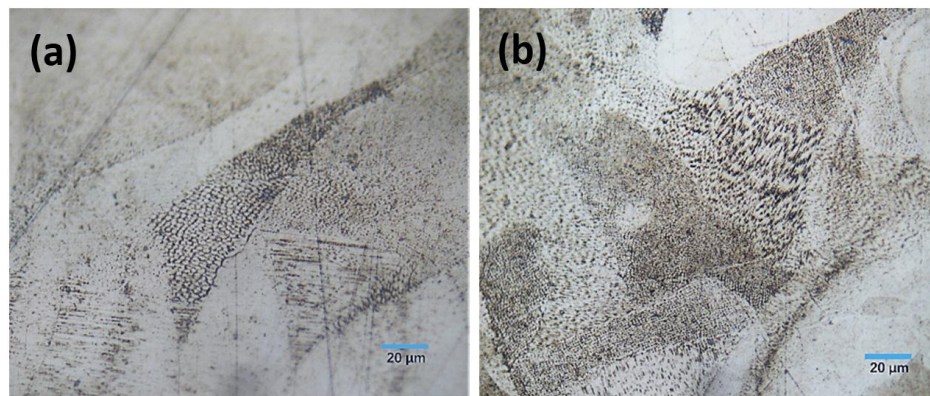

Figure 3. (**a**) and (**b**) show fine cellular-dendritic microstructures in SLM-fabricated 316L SS specimens.

It is well understood that the microstructures obtained in AM-processed metal parts, which depend on the applied processing parameters, strongly influence the mechanical properties of the parts, e.g., the densification levels, yield and tensile strengths and microhardness. Furthermore, the fine microstructures obtained via AM processes lead to improvements in tensile strength and microhardness compared to conventional manufacturing techniques [28,29].
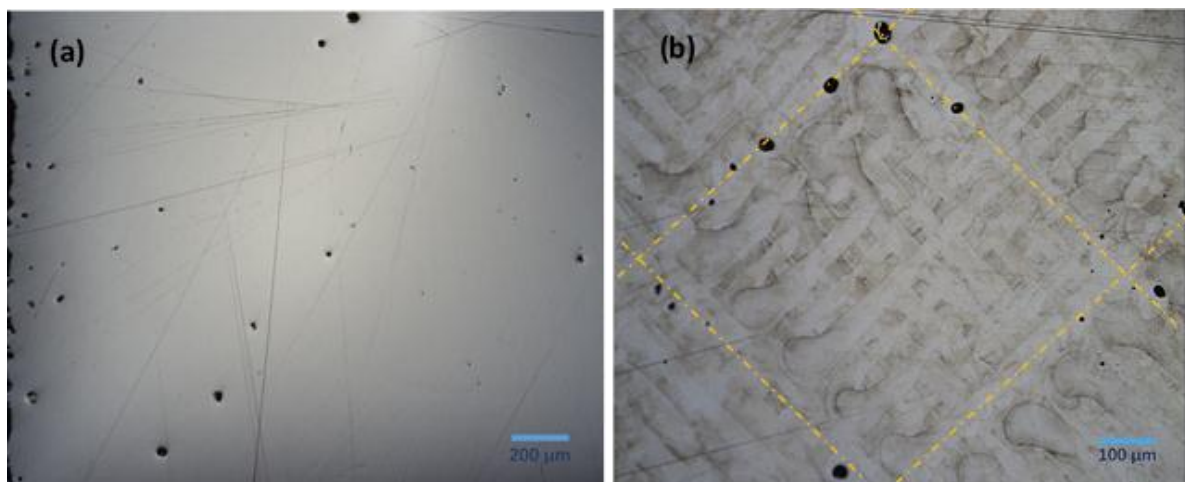
3.2. Porosity

Figure 4 shows the average pore size distribution in the AM 316L SS samples obtained by optical microscopy. The pore sizes ranged from ~5 μm to ~45 μm, where the smaller pores (≤5 μm) accounted for the majority (~60%) and the larger pores (>30 μm) accounted for less than 3%. The average porosity of the SLM specimens was calculated to be 0.82% ± 0.36%, which means that a high densification level (≥99%) was achieved.
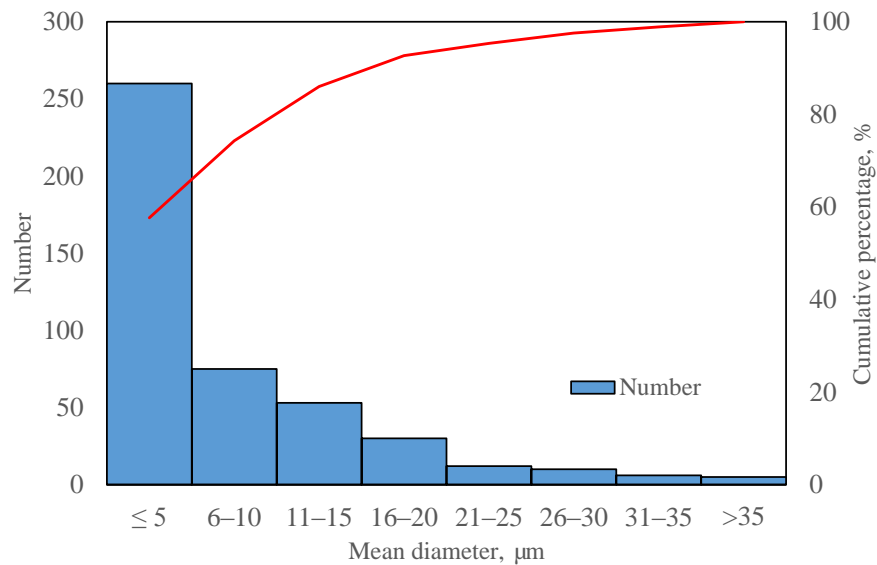
Figure 4. Pore size distribution in SLM samples, obtained from optical microscopy. Red curve represents the cumulative pore distribution.

However, the pores were not evenly distributed throughout the cut specimens and some of them were concentrated more in certain areas compared to others. It was observed that for the samples cut along the *x*–*y* plane (along the scan direction), the pores were mainly concentrated at the boundary of the "island" which was employed as the scan strategy during SLM in this study (Figure 5). In other words, the pores were located at the overlapping area between two "islands", similar to the work carried out by Gustmann et al. [30]. Interestingly, aligned pores appeared regularly along the build direction for the samples cut along the *x*–*z* and *y*–*z* planes (Figure 6). This could be the result of inclusions such as oxides present upon solidification of the molten pool [31–33]. Nevertheless, the porosity content at these regions with a high porosity concentration amounted up to ~1.68%, which is still a small figure as a whole but is relatively higher than the average porosity content calculated.


Figure 5. Micrographs showing porosity distribution for the (**a**) un-etched and (**b**) etched specimen cut along the *x*–*y* plane.
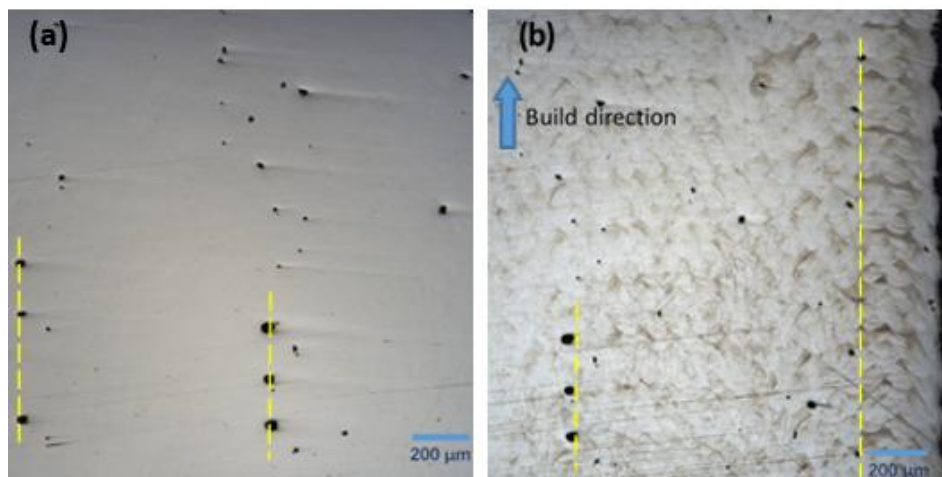
Figure 6. Aligned pores at successive solidified layers for: (**a**) un-etched and (**b**) etched specimens cut along the *x*–*z* plane. Similar results were observed for specimens in the *y*–*z* plane.

On the other hand, after the initial scanning of one SLM sample which had a relatively complex geometry (Figure 7a) by using advanced X-ray computed tomography (XCT) under a low resolution, a small region near the inner circle profile of the sample was found to have the highest porosity content compared to other regions throughout the sample (Figure 7b). Through detailed scanning of this region under high resolution, the porosity content was found to be 0.61%, with pore sizes ranging from 5 μm to ~74 μm, as shown in Figure 8. The porosity content in the scanned region was also not evenly distributed, with the majority of the pores concentrated close to the surface (inner wall) of the scanned region (Figure 9). However, a comparative study on porosity could not be carried out because only one sample was subjected to the XCT scan. Hence, the results obtained were not representative for all 316L SS samples fabricated by SLM.
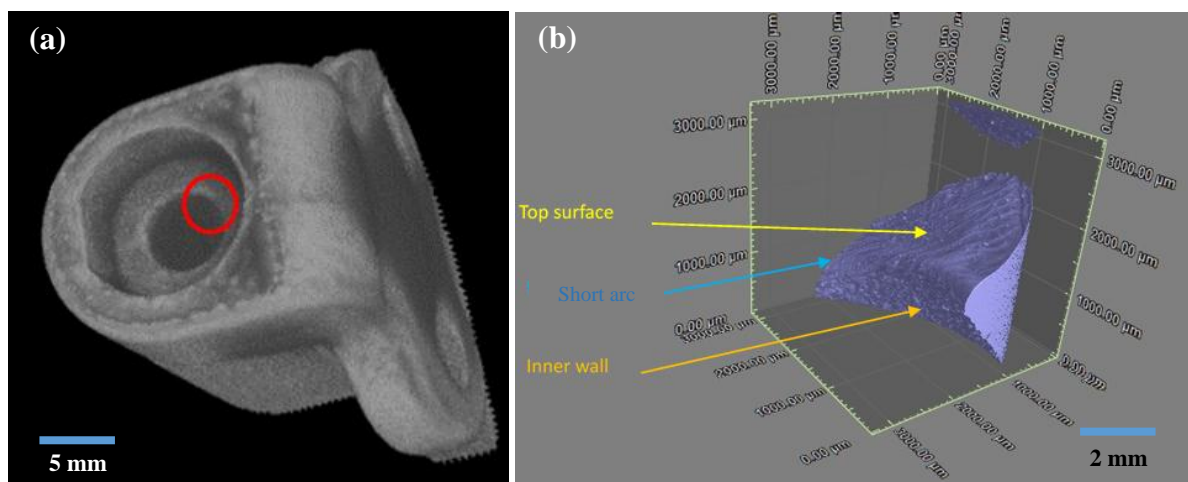
Figure 7. (**a**) Three-dimensional view of the AM-fabricated sample with a relatively complex geometry; (**b**) 3D view of the small region near the inner circle profile (red circle in 7a) further observed under high resolution.
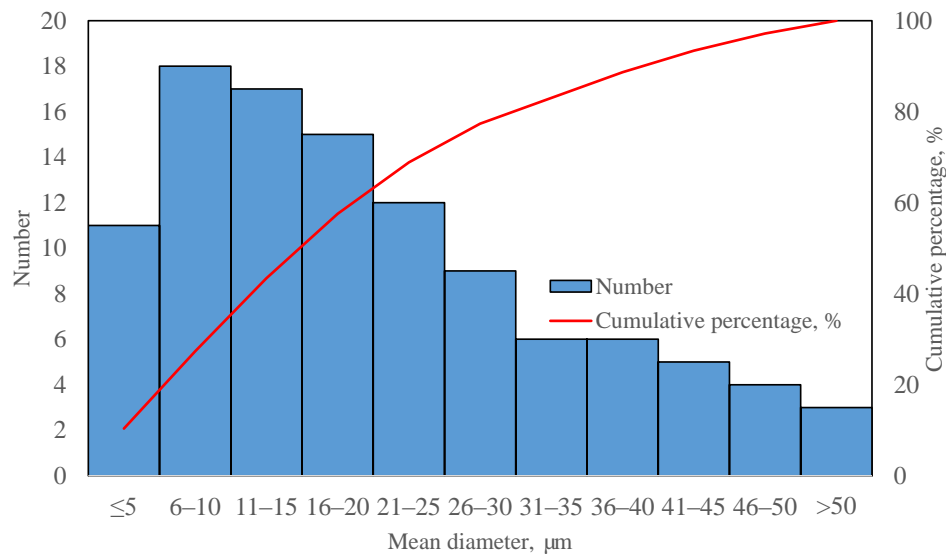
Figure 8. Pore size distribution for SLM sample shown in Figure 7b, obtained via XCT scan. Red curve represents the cumulative pore distribution.
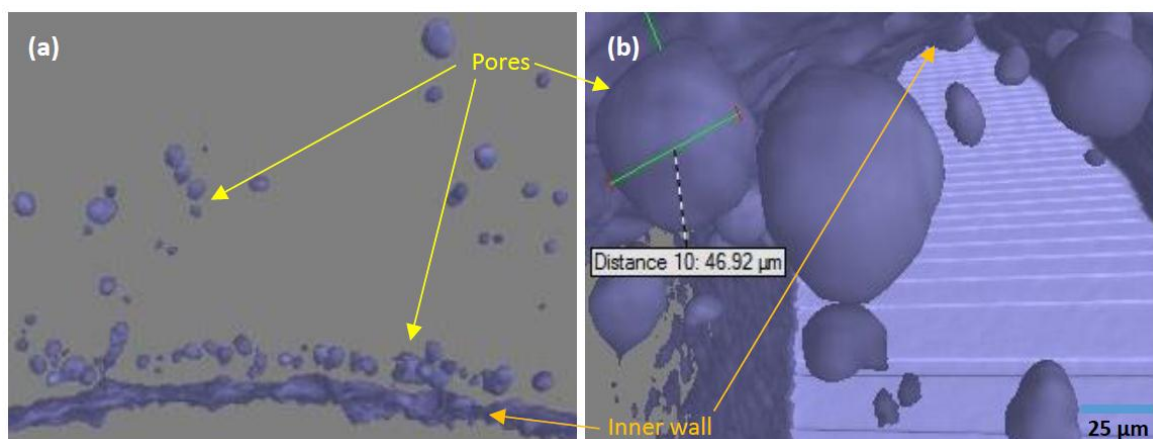
Figure 9. (**a**) Majority of the pores in the CT-scanned sample were observed close to the surface (inner wall) of the region in study; (**b**) Example of pore shape and size near the inner wall region.

Nevertheless, the XCT scan could be a better method to study the porosity distribution in AM-fabricated samples. This is because it is a non-destructive technique which enables detailed 3D visualisation of internal pores in the samples (Figure 9) without physically and chemically disrupting the sample, as compared to the conventional metallographic preparation for optical microscopy observation. However, only a small percentage of small pore sizes (<5 μm mean diameter) could be captured with the 3.2 μm resolution of the XCT scan used in this study compared to those obtained using optical microscopy. In addition, a much higher cost and longer time are required to obtain a higher resolution to detect smaller pore sizes, which is the current limitation of this technology.

Porosity is a common defect observed in the AM of metal parts, and it can be controlled by adjusting various processing parameters, e.g., the scan speed, laser power and layer thickness. In general, there are two types of porosities including gas-induced porosity and process-induced porosity [34]. Spherical-shaped gas pores could arise during the gas atomisation of the 316L SS feedstock material prior to SLM processing and continue to be present in the final parts. On the other hand, pores resulting from process-induced porosity are typically non-spherical. They are formed when either: (a) the energy applied is insufficient to completely melt the powder feedstock, causing

lack of fusion between each adjacent scan and between successive layers [35]; or (b) excessive energy is applied, resulting in spatter ejection [36]. In this study, spherical pores dominated the non-spherical ones, where rectangular-shaped pores were visible only near the edges of the cut specimens. This indicates that most of the porosity defects in the SLM samples were due to gas pores during the gas atomisation of the 316L SS powders, similar to the work carried out by Tammas-Williams et al. [37]. The gas pores could be produced due to the presence of moisture or contaminants on the surface of the powder particles [38]. These pores could also be formed by the reactions between O_2 and C which are present in small amounts during SLM processing, causing CO or CO_2 gas entrapment in the SLM-built parts [39]. The non-uniform pore distribution in this process could be caused by one of the following factors: (i) the variation of surface roughness [40]; and (ii) the layer-wise build manner of the AM [41]. The variation in surface roughness results in an inhomogeneous powder distribution that leads to an inconsistent melt flow and an unstable molten pool in the successive layers [42]. These, in turn, contribute to the discontinuities in the scan track formation, and hence the irregular pore distribution obtained in this study. Nevertheless, these defects (pores and voids) are detrimental to the quality of AM-fabricated metal parts, especially as they reduce mechanical properties such as yield and tensile strength.

3.3. Microhardness

The results of the Vickers microhardness (HV) tests were evaluated by: (i) comparing HV values of SLM samples for different cut planes (*x*–*y*, *x*–*z* and *y*–*z*) as shown in Figure 10; and (ii) comparing HV values of SLM and WM samples (Figure 11).
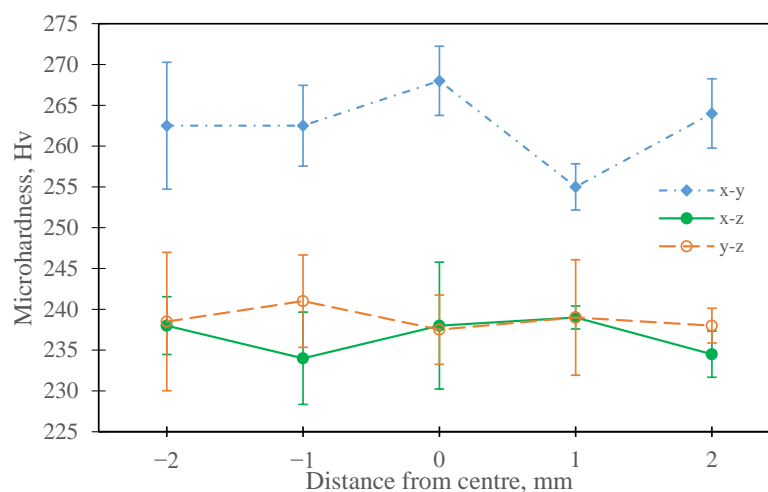
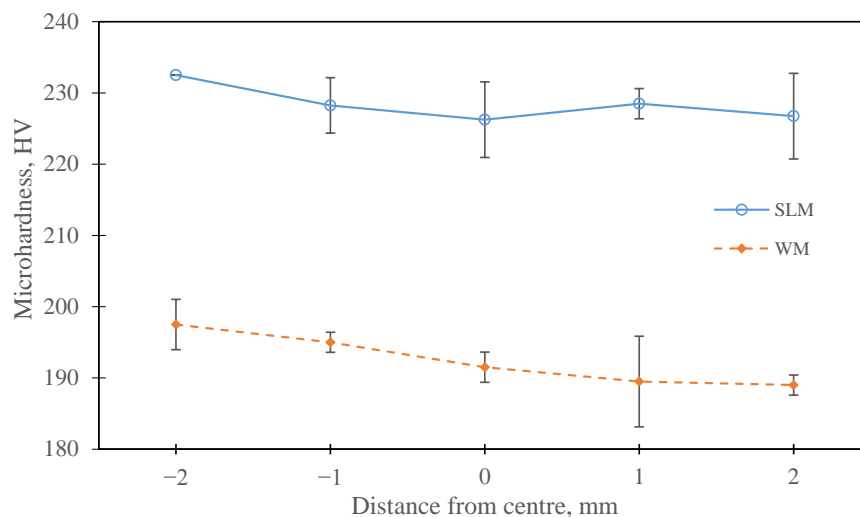
Figure 10. Average microhardness (HV) values for SLM specimens in the *x*–*y*, *x*–*z* and *y*–*z* planes.

From Figure 10, it can be observed that the average microhardness values for the SLM specimens in *x*–*y*, *x*–*z* and *y*–*z* planes are 262 HV, 237 HV, and 239 HV, respectively. The microhardness of the SLM samples at the *x*–*y* plane (scan direction) was the highest compared to the other two planes which had similar but considerably lower HV values. The discrepancy of the microhardness in each plane indicates anisotropy in SLM, which is typical of AM processes for metal components [28,43–45]. This is because of the layer-wise build approach with the "island" scan strategy in AM processes, which means localised melting of powder particles that often results in non-homogeneous morphologies and anisotropic grain structures [46,47]. However, the similar average HV values in the *x*–*z* and *y*–*z* planes indicated a more uniform microhardness distribution in the build direction compared to the scan direction for the SLM-processed samples. Figure 11 shows the average microhardness values of the SLM samples (228 HV), which were higher than those of the WM sample (192 HV). This is consistent with various literature, in which the microhardness of AM 316L SS parts is typically higher than that

of conventionally manufactured 316L SS parts [28,48]. Higher microhardness in AM 316L SS samples is attributed to the fine-grain microstructures obtained in the completed parts resulting in a higher dislocation density of austenite cells [49]. This makes slip motion along the grain boundaries difficult, thus increasing its strength and resistance to deformation. Although there is some porosity content in the SLM samples in this study, the defect is not expected to have a significant impact on the mechanical properties of the final part since the SLM processing was able to yield high densification levels (>99%) and the average porosity was also very low (~0.33%). Nevertheless, the porosity-microhardness relationship is an important aspect to consider when SLM is used to manufacture functional parts such as bone implants and industrial tools.

Figure 11. Average microhardness (HV) values for SLM and WM specimens.

4. Conclusions

The SLM-built 316L SS samples were able to achieve high densification levels (>99%) with a low average porosity content (~0.82%). Even though the porosity content in the SLM-built parts was very low, the pores were not evenly distributed throughout the samples. The highest porosity content in the concentrated regions was found to be ~1.68% which was higher than the overall average. Such low porosity content does not show an obvious impact on the mechanical properties of the AM 316L SS samples produced in this study. The higher average microhardness values of the SLM-fabricated 316L SS parts compared to their wrought manufactured counterpart were primarily attributed to the localised melting of the powder layers, and the rapid heating/cooling cycle involved during SLM contributed to the fine-grain microstructures in the completed parts.

Author Contributions: Shahir Mohd Yusuf analysed the data and wrote the manuscript; Yifei Chen carried out the experiments and analysed the data; Richard Boardman prepared and carried out the XCT scan; Shoufeng Yang and Nong Gao are experts in additive manufacturing (AM) and metallurgy, respectively, and they also managed and supervised the project.

Conflicts of Interest: The authors declare no conflict of interest.

References

1. Cherry, J.A.; Davies, H.M.; Mehmood, S.; Lavery, N.P.; Brown, S.G.R.; Sienz, J. Investigation into the effect of process parameters on microstructural and physical properties of 316L stainless steel parts by selective laser melting. *Int. J. Adv. Manuf. Technol.* **2014**, *76*, 869–879. [CrossRef]
2. Yusuf, S.M.; Gao, N. Influence of energy density on metallurgy and properties in metal additive manufacturing. *Mater. Sci. Technol.* **2017**. [CrossRef]

3. Guo, N.; Leu, M.C. Additive manufacturing: Technology, applications and research needs. *Front. Mech. Eng.* **2013**, *8*, 215–243. [CrossRef]

4. Zhang, L.C.; Attar, H. Selective Laser Melting of Titanium Alloys and Titanium Matrix Composites for Biomedical Applications: A Review. *Adv. Eng. Mater.* **2016**, *4*, 463–475. [CrossRef]

5. Frazier, W.E. Metal Additive Manufacturing: A Review. *J. Mater. Eng. Perform.* **2014**, *23*, 1917–1928. [CrossRef]

6. Gu, D.D.; Meiners, W.; Wissenbach, K.; Poprawe, R. Laser additive manufacturing of metallic components: Materials, processes and mechanisms. *Int. Mater. Rev.* **2012**, *57*, 133–164. [CrossRef]

7. Rafi, H.K.; Karthik, N.V.; Gong, H.; Starr, T.L.; Stucker, B.E. Microstructures and mechanical properties of Ti6Al4V parts fabricated by selective laser melting and electron beam melting. *J. Mater. Eng. Perform.* **2013**, *22*, 3872–3883. [CrossRef]

8. Liu, Y.J.; Li, S.J.; Wang, H.L.; Hou, W.T.; Hao, Y.L.; Yang, R.; Sercombe, T.B.; Zhang, L.C. Microstructure, defects and mechanical behavior of beta-type titanium porous structures manufactured by electron beam melting and selective laser melting. *Acta Mater.* **2016**, *113*, 56–67. [CrossRef]

9. Liu, Y.J.; Wang, H.L.; Li, S.J.; Wang, S.G.; Wang, W.J.; Hou, W.T.; Hao, Y.L.; Yang, R.; Zhang, L.C. Compressive and fatigue behavior of beta-type titanium porous structures fabricated by electron beam melting. *Acta Mater.* **2017**, *126*, 58–66. [CrossRef]

10. Liu, F.; Lin, X.; Yang, G.; Song, M.; Chen, J.; Huang, W. Microstructure and residual stress of laser rapid formed Inconel 718 nickel-base superalloy. *Opt. Laser Technol.* **2011**, *43*, 208–213. [CrossRef]

11. Riemer, A.; Leuders, S.; Thöne, M.; Richard, H.A.; Tröster, T.; Niendorf, T. On the fatigue crack growth behavior in 316L stainless steel manufactured by selective laser melting. *Eng. Fract. Mech.* **2013**, *120*, 15–25. [CrossRef]

12. Hao, L.; Dadbakhsh, S.; Seaman, O.; Felstead, M. Selective laser melting of a stainless steel and hydroxyapatite composite for load-bearing implant development. *J. Mater. Process. Technol.* **2009**, *209*, 5793–5801. [CrossRef]

13. Mathisen, M.B. In-Situ Tensile Testing Combined with EBSD Analysis of Ti-6Al-4V Samples from Components Fabricated by Additive Layer Manufacture. Master's Thesis, Norwegian University of Science and Technology, Trondheim, Norway, June 2012.

14. Yan, C.; Hao, L.; Hussein, A.; Young, P.; Raymont, D. Advanced lightweight 316L stainless steel cellular lattice structures fabricated via selective laser melting. *Mater. Des.* **2014**, *55*, 533–541. [CrossRef]

15. Verlee, B.; Dormal, T.; Lecomte-Beckers, J. Density and porosity control of sintered 316L stainless steel parts produced by additive manufacturing. *Powder Metall.* **2012**, *55*, 260–267. [CrossRef]

16. Dewidar, M.; Khalil, A.; Lim, J.K. Processing and mechanical properties of porous 316L stainless steel for biomedical applications. *Trans. Nonferr. Met. Soc. China* **2007**, *17*, 468–473. [CrossRef]

17. AlMangour, B.; Grzesiak, D.; Yang, J.M. Selective laser melting of TiC reinforced 316L stainless steel matrix nanocomposites: Influence of starting TiC particle size and volume content. *Mater. Des.* **2016**, *104*, 141–151. [CrossRef]

18. AlMangour, B.; Grzesiak, D.; Yang, J.M. Rapid fabrication of bulk-form TiB2/316L stainless steel nanocomposites with novel reinforcement architecture and improved performance by selective laser melting. *J. Alloy. Compd.* **2016**, *680*, 480–493. [CrossRef]

19. AlMangour, B.; Grzesiak, D.; Yang, J.M. Selective laser melting of TiB 2/316L stainless steel composites: The roles of powder preparation and hot isostatic pressing post-treatment. *Powder Technol.* **2017**, *309*, 37–48. [CrossRef]

20. Yasa, E.; Kruth, J.P. Microstructural investigation of Selective Laser Melting 316L stainless steel parts exposed to laser re-melting. *Proced. Eng.* **2011**, *19*, 389–395. [CrossRef]

21. Jinhui, L.; Ruidi, L.; Wenxian, Z.; Liding, F.; Huashan, Y. Study on formation of surface and microstructure of stainless steel part produced by selective laser melting. *Mater. Sci. Technol.* **2010**, *26*, 1259–1264. [CrossRef]

22. Carter, L.N.; Martin, C.; Withers, P.J.; Attallah, M.M. The influence of the laser scan strategy on grain structure and cracking behaviour in SLM powder-bed fabricated nickel superalloy. *J. Alloy. Compd.* **2014**, *615*, 338–347. [CrossRef]

23. Thijs, L.; Kempen, K.; Kruth, J.P.; van Humbeeck, J. Fine-structured aluminium products with controllable texture by selective laser melting of pre-alloyed AlSi10Mg powder. *Acta Mater.* **2013**, *61*, 1809–1819. [CrossRef]

24. Otsu, N. A threshold selection method from gray-level histograms. *IEEE Trans. Syst. Man. Cybern.* **1979**, *9*, 62–66. [CrossRef]

25. Lu, Y.; Wu, S.; Gan, Y.; Huang, T.; Yang, C.; Junjie, L.; Lin, J. Study on the microstructure, mechanical property and residual stress of SLM Inconel-718 alloy manufactured by differing island scanning strategy. *Opt. Laser Technol.* **2015**, *75*, 197–206. [CrossRef]

26. Zhou, X.; Li, K.; Zhang, D.; Liu, X.; Ma, J.; Liu, W.; Shen, Z. Textures formed in a CoCrMo alloy by selective laser melting. *J. Alloy. Compd.* **2015**, *631*, 153–164. [CrossRef]

27. Hedberg, Y.S.; Qian, B.; Shen, Z.; Virtanen, S.; Odnevall Wallinder, I. In vitro biocompatibility of CoCrMo dental alloys fabricated by selective laser melting. *Dent. Mater.* **2014**, *30*, 525–534. [CrossRef] [PubMed]

28. Zietala, M.; Durejko, T.; Polanski, M.; Kunce, I.; Plocinski, T.; Zielenski, W.; Lazinska, M.; Stepniowski, W.; Czujko, T.; Kurzydlowski, K.J.; et al. The microstructure, mechanical properties and corrosion resistance of 316L stainless steel fabricated using laser engineered net shaping. *Mater. Sci. Eng. A* **2016**, *677*, 1–10. [CrossRef]

29. Zhong, Y.; Liu, L.; Wikman, S.; Cui, D.; Shen, Z. Intragranular cellular segregation network structure strengthening 316L stainless steel prepared by selective laser melting. *J. Nucl. Mater.* **2016**, *470*, 170–178. [CrossRef]

30. Gustmann, T.; Neves, A.; Kühn, U.; Gargarella, P.; Kiminami, C.S.; Bolfarini, C.; Eckert, J.; Pauly, S. Influence of processing parameters on the fabrication of a Cu-Al-Ni-Mn shape-memory alloy by selective laser melting. *Addit. Manuf.* **2016**, *11*, 23–31. [CrossRef]

31. Marya, M.; Singh, V.; Marya, S.; Hascoet, J.Y. Microstructural Development and Technical Challenges in Laser Additive Manufacturing: Case Study with a 316L Industrial Part. *Metall. Mater. Trans. B Process Metall. Mater. Process. Sci.* **2015**, *46*, 1654–1665. [CrossRef]

32. Liu, Z.H.; Zhang, D.Q.; Sing, S.L.; Chua, C.K.; Loh, L.E. Interfacial characterization of SLM parts in multi-material processing: Metallurgical diffusion between 316L stainless steel and C18400 copper alloy. *Mater. Charact.* **2014**, *94*, 116–125. [CrossRef]

33. Dadbakhsh, S.; Hao, S. Effect of Al alloys on selective laser melting behaviour and microstructure of in situ formed particle reinforced composites. *J. Alloy. Compd.* **2012**, *541*, 328–334. [CrossRef]

34. Sames, W.J.; List, F.A.; Pannala, S.; Dehoff, R.R.; Babu, S.S. The metallurgy and processing science of metal additive manufacturing. *Int. Mater. Rev.* **2016**, *6608*, 1–46. [CrossRef]

35. King, W.E.; Barth, H.D.; Castillo, V.M.; Gallegos, G.F.; Gibbs, J.W.; Hahn, D.E.; Kamath, C.; Rubenchik, A.M. Observation of keyhole-mode laser melting in laser powder-bed fusion additive manufacturing. *J. Mater. Process. Technol.* **2014**, *214*, 2915–2925. [CrossRef]

36. Körner, C.; Bauereiß, A.; Attar, E. Fundamental consolidation mechanisms during selective beam melting of powders. *Model. Simul. Mater. Sci. Eng.* **2013**, *21*, 1–18. [CrossRef]

37. Tammas-Williams, S.; Zhao, H.; Léonard, F.; Derguti, F.; Todd, I.; Prangnell, P.B. XCT analysis of the influence of melt strategies on defect population in Ti-6Al-4V components manufactured by Selective Electron Beam Melting. *Mater. Charact.* **2015**, *102*, 47–61. [CrossRef]

38. Frazier, W.E. Direct digital manufacturing of metallic components: Vision and roadmap. In Proceedings of the 21st Annual International Solid Freeform Fabrication Symposium, Austin, TX, USA, 9–11 August 2010; pp. 717–732.

39. Campanelli, S.L.; Contuzzi, N.; Angelastro, A.; Ludovico, A.D. Capabilities and Performances of the Selective Laser Melting Process. In *New Trends in Technologies: Devices, Computer, Communication and Industrial Systems*; Er, M.J., Ed.; InTech Europe: Rijeka, Croatia, 2010; pp. 233–252.

40. Qiu, C.; Panwisawas, C.; Ward, M.; Basoalto, H.C.; Brooks, J.W.; Attallah, M.M. On the role of melt flow into the surface structure and porosity development during selective laser melting. *Acta Mater.* **2015**, *96*, 72–79. [CrossRef]

41. Maskery, I.; Aboulkhair, N.T.; Corfield, M.R.; Tuck, C.; Clare, A.T.; Leach, R.K.; Wildman, R.D.; Ashcroft, I.A.; Hague, R.J.M. Quantification and characterisation of porosity in selectively laser melted Al-Si10-Mg using X-ray computed tomography. *Mater. Charact.* **2016**, *111*, 193–204. [CrossRef]

42. Kang, N.; Coddet, P.; Liu, Q.; Liao, H.; Coddet, C. In-situ TiB/near α Ti matrix composites manufactured by selective laser melting. *Addit. Manuf.* **2016**, *11*, 1–6. [CrossRef]

43. Niendorf, T.; Leuders, S.; Riemer, A.; Richard, H.A.; Tröster, T.; Schwarze, D. Highly anisotropic steel processed by selective laser melting. *Metall. Mater. Trans. B Process Metall. Mater. Process. Sci.* **2013**, *44*, 794–796. [CrossRef]

44. Qiu, C.; Adkins, N.J.E.; Attallah, M.M. Microstructure and tensile properties of selectively laser-melted and of HIPed laser-melted Ti-6Al-4V. *Mater. Sci. Eng. A* **2013**, *578*, 230–239. [CrossRef]

45. Dai, N.; Zhang, L.C.; Zhang, J.; Zhang, X.; Ni, Q.; Chen, Y.; Wu, M.; Yang, C. Distinction in corrosion resistance of selective laser melted Ti-6Al-4V alloy on different planes. *Corros. Sci.* **2016**, *111*, 703–710. [CrossRef]

46. Wu, A.S.; Brown, D.W.; Kumar, M.; Gallegos, G.F.; King, W.E. An Experimental Investigation into Additive Manufacturing-Induced Residual Stresses in 316L Stainless Steel. *Metall. Mater. Trans. A Phys. Metall. Mater. Sci.* **2014**, *45*, 6260–6270. [CrossRef]

47. Thijs, L.; Montero Sistiaga, M.L.; Wauthle, R.; Xie, Q.; Kruth, J.P.; van Humbeeck, J. Strong morphological and crystallographic texture and resulting yield strength anisotropy in selective laser melted tantalum. *Acta Mater.* **2013**, *61*, 4657–4668. [CrossRef]

48. Tolosa, I.; Garciandía, F.; Zubiri, F.; Zapirain, F.; Esnaola, A. Study of mechanical properties of AISI 316 stainless steel processed by "selective laser melting", following different manufacturing strategies. *Int. J. Adv. Manuf. Technol.* **2010**, *51*, 639–647. [CrossRef]

49. Saeidi, K.; Gao, X.; Zhong, Y.; Shen, Z.J. Hardened austenite steel with columnar sub-grain structure formed by laser melting. *Mater. Sci. Eng. A* **2015**, *625*, 221–229. [CrossRef]